



Investigation of the Long-term Stability of Solid Oxide Electrolysis Stacks under Pressurized Conditions in Exothermic Steam and Co-electrolysis Mode

M. Riedel^{1*}, M. P. Heddrich¹, K. A. Friedrich^{1,2}

¹ German Aerospace Center (DLR), Institute of Engineering Thermodynamics, Pfaffenwaldring 38–40, 70569 Stuttgart, Germany

² University of Stuttgart, Institute of Building Energetics, Thermal Engineering and Energy Storage (IGTE), Pfaffenwaldring 31, 70569 Stuttgart, Germany

Received February 11, 2020; accepted May 18, 2020; published online September 01, 2020

Abstract

In this study three identically constructed ten-layer stacks with electrolyte supported cells were tested in exothermic steam and co-electrolysis mode at elevated pressures of 1.4 and 8 bar. Investigations during constant-current operation at a current density of -0.5 A cm^{-2} and a reactant conversion of 70% over 1,000–2,000 h were carried out. The inlet gas composition for steam electrolysis was 90/10 ($\text{H}_2\text{O}/\text{H}_2$) and 63.7/31.3/3.3/1.7 ($\text{H}_2\text{O}/\text{CO}_2/\text{H}_2/\text{CO}$) for co-electrolysis operation. All stacks showed highly similar resistances at the beginning of the tests indicating a high level of accuracy and repeatability during manufacturing. The stack operated in steam electrolysis mode at 1.4 bar showed comparably low degradation of $8 \text{ mV kh}^{-1} \text{ cell}^{-1}$, whereas the stack operated at 8 bar showed an approximately four times higher degrada-

tion. The third stack was operated in co-electrolysis mode at 1.4 and 8 bar and showed noticeably higher degradation rates than during steam electrolysis mode. The predominant increase of the ohmic resistance during operation was identified to be mainly responsible for the observed degradation of all three stacks, whereas the increase of the polarization resistances played a subordinate role. Within the post-test analysis, noticeably high nickel depletion was observed for the stack operated at the highest pressure in steam electrolysis mode. Furthermore, partial delamination of electrodes was observed. The degradation is discussed with relation to phenomena and experimental parameters during operation.


Keywords: Degradation, Pressure, Solid Oxide Electrolysis Cell, SOEC, 10-cell Stack

1 Introduction

Solid oxide electrolyzers are known as efficient energy converters for producing hydrogen or synthesis gas (H_2+CO) from steam and/or CO_2 . Due to the high operating temperatures, solid oxide electrolysis cells (SOECs) offer significant benefits in terms of fast kinetics, reduced electrochemical losses and high electrical-to-chemical conversion efficiencies. Furthermore, the produced hydrogen or synthesis gas can be used as feedstock for the production of base chemicals or synthetic fuels in downstream processes like Fischer-Tropsch or methanol synthesis. However, the respective downstream reactors are typically operated at elevated pressures in the range of 10 to 60 bar to achieve high conversion or high yield. Since the cell performance was already shown to improve due

to reduced overpotentials the combination of SOEC stacks and the downstream reactors in one pressurized system could be highly beneficial [1–3]. However, studies investigating the performance of stacks with electrolyte supported cells showed that the influence of pressurized operation on the electrochemical performance is low [4–7]. The decrease of overpotentials

[*] Corresponding author, Marc.Riedel@dlr.de

 This is an open access article under the terms of the Creative Commons Attribution-NonCommercial License, which permits use, distribution and reproduction in any medium, provided the original work is properly cited and is not used for commercial purposes.

may not be high compared to the pressurized operation of cathode supported cell concepts. Nevertheless, the direct coupling of SOECs to downstream processes can lead to additional advantages on system level. For instance, liquid water and CO₂ compression need significantly less energy than steam, hydrogen or syngas compression [1, 8]. Furthermore, the coupling of the electrolysis and synthesis processes enable close process integration and intensification synergies like significantly reduced or omitted compression work of the produced hydrogen or syngas before entering the downstream synthesis. However, certain challenges related to the design and the operation of pressurized SOECs and combined systems have to be considered. Increased pressure differences between anode, cathode or the surrounding atmosphere have to be avoided since it can lead to the destruction of the electrochemical device [9]. Furthermore, the produced oxygen on the anode side has to be flushed from the electrode and individual safety restrictions related to the maximum oxygen concentration in the outlet can lead to significant use of air, N₂ or CO₂ for dilution. A compression of the flushing medium and its recirculation could be required in order to avoid severe losses in process efficiency. These criteria have to be considered and evaluated for each individual system need.

However, both pressurized and non-pressurized SOEC systems with relevant power output are still under development and need to fulfill certain criteria to become of broad economic and commercial interest. The performance stability of the stacks in long-term operation is one of the key factors for competitiveness and the feasibility to enter into mass market.

On cell level several experimental studies were carried out and degradation mechanisms were already proposed [10–15]. However, the reported degradation data are mostly hard to compare since cell concepts, materials and experimental conditions such as reactant flows, gas composition, conversion, voltage or current density strongly differ from one study to the other. Experimental investigations on the long-term stability of SOEC stacks are less available but highly required to identify and promote potential developments on cell, stack or system level [5, 16–23].

In this study, three identically constructed ten-layer stacks with electrolyte supported cells were tested in exothermic steam and co-electrolysis mode at elevated pressures of 1.4 and 8 bar. Investigations during constant-current operation over 1,000–2,000 h were carried out. Electrochemical impedance spectroscopy (EIS) and post-test analysis (PTA) *via* scanning electron microscopy (SEM) and energy-dispersive X-ray spectroscopy (EDX) was used, in order to identify the influence of the operating pressure on the performance stability and microstructural changes of the cells in more detail.

2 Experimental

In order to investigate the long-term stability of SOCs operated at different pressures, three commercially available stacks with ten electrolyte supported cells (ESC) were evaluated.

Each cell has an active area of 127.8 cm² and consists of an approximately 55 μm thick lanthanum strontium cobalt ferrite oxide (LSCF) oxygen electrode, a 90 μm thick yttria-stabilized zirconia (3YSZ) electrolyte and a 30 μm thick nickel gadolinia-doped ceria (Ni-GDC) composite as fuel electrode. Additionally, a thin GDC layer is used between the electrolyte/fuel electrode and the electrolyte/air electrode, respectively.

Within this study, constant-current long-term tests were performed both in steam electrolysis and co-electrolysis mode. The pure steam electrolysis operation was examined with two stacks over 1,000 h at 1.4 bar, and over 2,000 h at 8 bar. Within these experiments an inlet gas composition with molar fractions of 90% H₂O and 10% H₂ was used. The third stack was mainly investigated in co-electrolysis mode at two different pressures (1.4 and 8 bar) with an inlet gas composition with molar fractions of 63.7% H₂O, 31.3% CO₂, 3.3% of H₂, and 1.7% CO. However, the first 160 h were conducted in steam electrolysis mode to enable comparability. All experiments were performed at a furnace temperature of 800 °C and a current density of -0.5 A cm^{-2} . The inlet mass flows were set for a constant reactant conversion (RC) of 70%. Table 1 gives an overview about the stacks A–C used in this study and the associated experiments.

The stacks are housed into gas tight steel boxes due to the open oxygen electrode design of each repeating unit. Each repeating unit of the stack consists of two fuel gas inlets and two fuel gas outlets. Along the cell length, gas channels within the fuel electrode and air electrode compartment distribute the media in co-flow condition. More details about the stack configuration with modeling and experimental results of the temperature distribution along and across the stack and its repeating units can be found elsewhere [24–26]. During the experiments the oxygen electrodes of each stack were flushed with 1 slpm per cell air to prevent the accumulation of pure oxygen with its corrosive characteristic in the outlet pipes of the testing facility. This led to an oxygen outlet content of 36% at the defined operating point with 70% of reactant conversion. For measuring the temperatures inside the stack during operation, an overall number of five thermocouples with a diameter of 0.25 mm are placed directly on certain oxygen electrode layers. However, the thin thermocouples sometimes fail due to mechanical stress inside the steel box. As Figure 1 shows, one thermocouple each is placed at the middle length of layer one and layer ten. The remaining three thermocouples are placed at quarter, half and three-quarter lengths of layer five. Due to test housing restrictions, the ten cells within the stacks of this study are electrically packaged into five cell

Table 1 Overview of the experiments conducted with the three stacks A–C.

Description	Operation mode	Pressure / bar	Duration / h
Stack A	Steam electrolysis	1.4	1,000
Stack B	Steam electrolysis	8	2,000
Stack C	Steam & Co-electrolysis	1.4 and 8	1,000

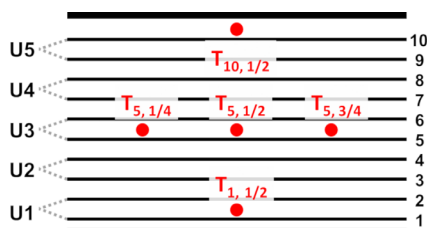


Fig. 1 Sketch of the 10-layer stack with the positioning of the five thermocouples ($T_{i,j}$) and a depiction of the electrical packaging into five cell blocks.

blocks. Hence, the cell voltages of two cells are measured in series. A further description of the pressurized test facility as well as the design of the stack housing can be found elsewhere [5, 7].

In order to monitor the outlet gas composition during the co-electrolysis experiment, a Rosemount X-Stream analyzer with sensors for H_2 , CO , CO_2 , and CH_4 is connected to the test facility. Due to the measuring principle of this analyzer, the steam of the gas mixture is removed *via* a compressor chiller operated at $3^\circ C$. All gases can be analyzed in a range of 0–100% with an accuracy of $\leq \pm 1\%$ points.

At the beginning of the tests and several times within the experiment, electrochemical impedance spectroscopy (EIS) was carried out at the operating point, in order to evaluate the time-dependent change of the resistances. The frequency range was from 0.05 Hz to 20 kHz with ten points per decade and an amplitude of 0.96 A. The impedance spectra were recorded using a Zahner Zennium impedance analyzer. After the degradation tests, the three stacks were disassembled and the middle cells of the stacks were used for post-test analysis *via* scanning electron microscopy (SEM) and energy-dispersive X-ray spectroscopy (EDX).

3 Results and Discussion

The increased partial pressure of the reactants under pressurized operation leads to an increased Nernst voltage, due to well-known thermodynamic relations [2]. In order to secure exact measurements, the open circuit voltages (OCV) of all the three stacks were monitored and compared with the theoretical Nernst voltages (U_{Nernst}) at $800^\circ C$ before starting the long-term experiments. For stack A and B a gas composition of 90/10 (H_2O/H_2), for stack C the co-electrolysis mixture of 63.7/31.3/3.3/1.7 ($H_2O/CO_2/H_2/CO$) was used. Note that the table presents the voltages of two layers due to the described electrical series connection of two cells within the stacks.

As shown within Table 2, the OCVs of all stacks are in good agreement with the theoretical (doubled) Nernst voltage indicating an exact dosage of the gas flows for all experiments and negligible leakages inside the

studied stacks. However, stack A shows an apparent deviation of the four upper layers with a significantly decreased OCV. Though these cells showed low voltages during non-loaded conditions, the measured temperatures within the stack did not exceed furnace temperature. This would be clearly noticeable in case of a cell crack and corresponding oxidation of the hydrogen content of the feed in the anode or cathode compartment. Furthermore, the four upper layers did not show any negative influence on the overall stack performance during operation over 1,000 h (see Section 3.1). Hence, one can assume that the apparent low voltages of the cells were caused by electrical wiring problems within the testing facility. Apart from these layers of stack A, the maximum deviation between the experimentally obtained and theoretically calculated block voltage is 1 mV for stack A, 4 mV for stack B, and 6 mV for stack C.

Figure 2 shows the ohmic resistance of each stack at the operating current density of $-0.5 A cm^{-2}$ with its predefined gas composition before the start of the long-term tests. The depicted temperature was measured with the thermocouple placed at the middle length of the air electrode of layer 5 ($T_{5,1/2}$). It was already shown by the authors that this temperature can be taken as the characteristic stack temperature in steam electrolysis mode [5]. The ohmic resistance of stack A showed a value of $0.670 \Omega cm^2$ at a characteristic temperature of $825.3^\circ C$. Stack B and stack C showed characteristic

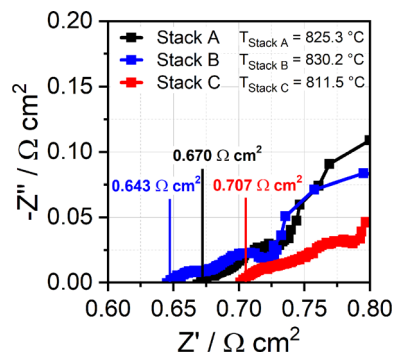


Fig. 2 Impedance spectra of the three stacks at constant-current operation ($-0.5 A cm^{-2}$) before the long-term tests. Stack A is operated at 1.4 bar, stack B at 8 bar in steam electrolysis mode and stack C is operated in co-electrolysis mode at 1.4 bar.

Table 2 OCV values of the three stacks with an inlet gas composition of 90/10 (H_2O/H_2) for stack A (1.4 bar) and B (8 bar) and 63.7/31.3/3.3/1.7 ($H_2O/CO_2/H_2/CO$) for stack C (1.4 bar). The values in brackets indicate the (averaged) single cell voltages.

	Voltage stack A / V (single cell voltage / V)	Voltage stack B / V (single cell voltage / V)	Voltage stack C / V (single cell voltage / V)
Theoretical voltage	1.695 (0.848)	1.776 (0.888)	1.628 (0.814)
Layer 1+2	1.694 (0.847)	1.779 (0.890)	1.623 (0.812)
Layer 3+4	1.695 (0.848)	1.779 (0.890)	1.622 (0.811)
Layer 5+6	1.694 (0.847)	1.780 (0.890)	1.624 (0.812)
Layer 7+8	0.820 (0.410)*	1.778 (0.889)	1.624 (0.812)
Layer 9+10	0.748 (0.374)*	1.780 (0.890)	1.623 (0.812)

temperatures of 830.2 °C and 811.5 °C, and ohmic resistances of 0.643 Ω cm² and 0.707 Ω cm², respectively. The measured ohmic resistances of the stacks at the defined operating point correlate well with the temperature dependency published in [5].

The differences of the ohmic resistances can be attributed to the different operating conditions of the stacks. In particular, stack B is operated at higher pressure leading to a higher voltage and consequently a higher temperature. Stack C operates at a reduced temperature due to the additionally occurring endothermic reversed water-gas shift (rWGS) reaction while operating in co-electrolysis mode. Hence, it can be concluded that all the studied stacks show highly similar resistances at the beginning of the tests indicating a decent level of accuracy and repeatability during manufacturing.

3.1 1,000 h Steam Electrolysis Operation at 1.4 bar

Figure 3 shows the result of the first long-term test over 1,000 h at an operating pressure of 1.4 bar in steam electrolysis mode. At the current density of -0.5 A cm^{-2} and a furnace temperature of 800 °C the ESC stack is operated exothermically at approximately 1.33 V per cell at the start of the test. The values shown for the single cell voltage are derived from the layers 5+6 of the ten-layer stack, whereas the measured temperature was derived from $T_{5,1/2}$. The total area specific resistance (ASR_{total}) was calculated at steady state condition based on the single cell voltage and the averaged theoretical Nernst voltage ($U_{\text{Nernst, avg}}$) at the applied current density:

$$ASR_{\text{total}} = (U_{\text{measured}} - U_{\text{Nernst, avg}}) / i \quad (1)$$

The Nernst voltage is determined according to the averaged gas composition between the inlet and the outlet of the

stack [4]. Due to the analysis shown in Table 1 and the derived negligibility of leakages inside the stacks, assuming the outlet gas composition to be defined purely by current and thermodynamic equilibrium is valid. $U(t)$ and $T(t)$ over 1,000 h can be found in a previous analysis by the authors [5]. However, the authors will focus on the analysis of the ASR behavior under the different experimental conditions shown within the current study and the comparison with the long-term tests of the identically constructed stacks B and C. As regards the completeness, the normalized ohmic resistance (ASR_{Ω}) and normalized polarization resistance (ASR_{pol}) are shown within the diagram according to the related results of the impedance study of Figure 5. The values of the ohmic resistance were obtained from the EIS data, whereas the polarization resistance was calculated as the difference between ASR_{total} and ASR_{Ω} , thus not considering the conversion recorded in EIS. The small voltage and temperature peaks which can be observed at every 200 h of operation are due to the switch between EIS analyzer and the load of the test rig. In contrast to the previous analysis, the time for the switch and the recording of the EIS spectra was not considered for the time of operation shown in Figure 3.

The voltage shows a nearly linear increase of 8 mV over the 1,000 h of operation. Accordingly, the ASR_{total} increases by 18 mΩ cm². Due to the increasing voltage, the characteristic cell temperature increases by 3.13 K kh⁻¹. The authors want to point out that contrary to the authors' previous studies and many other publications the degradation rates will not be given in percentages, since this specification is highly dependent on the operating voltage and can lead to wrong interpretation of the degradation [5, 14, 16–20, 27–31]. The indication of the shift in voltage and ASR during the operating time leads to much better comparability of experimental studies.

Figure 4a shows the behavior of the layers within this long-term experiment. As already shown by the results during OCV operation in Table 2, lower voltages of the layers 7+8 and 9+10 over the complete operating time were observed. Furthermore, the respective layers show a highly instable voltage behavior with a volatility of more than 200 mV. However, the remaining layers showed stable voltages over the complete operating time favoring the assumption of an electrical wiring issue within the testing facility of the layers 7+8 and 9+10. Layer 1+2 showed a rapidly decreasing voltage at around 400 h of operation. However, Figure 4b supports the hypothesis that this behavior was not caused by a crack in one of the cells or of some glass sealing since the thermocouple at the middle length of layer 1 ($T_{1,1/2}$) did not show any unduly behavior of the temperature. This indicates that the voltage decrease was likely caused by a loss of contact or a short circuit within the testing facility. The thermocouple $T_{1,1/2}$ broke completely approximately 100 h later. If the sensor failure of $T_{1,1/2}$ and the earlier observed decreased voltage of layer 1+2 may be related to each other, could not be finally clarified within the PTA. However, all remaining measured temperatures within the stack increased according to the cell voltages linearly over the 1,000 h of operation.

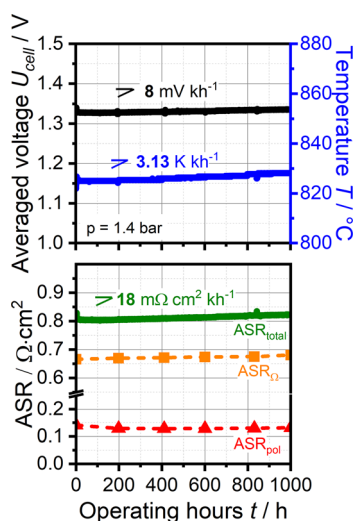


Fig. 3 Constant-current steam electrolysis operation over 1,000 h at 1.4 bar and 800 °C furnace temperature with stack A. The gas inlet composition was 90% H₂O with 10% H₂. The mass flow on the fuel side was set for a reactant conversion of 70% at a current density of -0.5 A cm^{-2} . $U(t)$ and $T(t)$ were taken from [5], normalized ohmic and polarization resistances were added according to the EIS and ASR analysis.

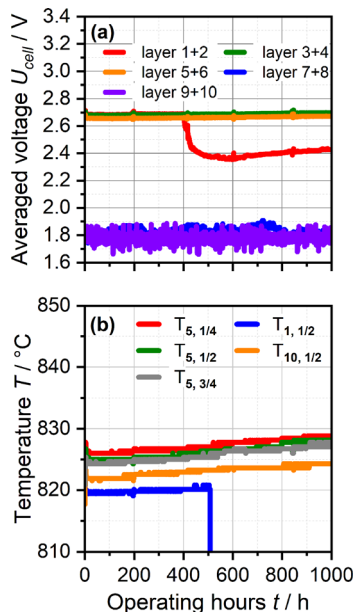


Fig. 4 a) Voltage behavior of the ten layers, and b) measured temperature trend within the stack A over 1,000 h of operation at 1.4 bar in constant-current steam electrolysis mode.

Table 3 gives an overview of the voltage and ASR shifts of stack A. As described earlier, the layers 1+2, 7+8, and 9+10 showed a conspicuous voltage behavior during the test and were not considered for evaluating the degradation rates (labelled with *). Hence, the averaged voltage shift per cell was 8 mV kh^{-1} and the ASR per cell increased by $18 \text{ m}\Omega \text{ cm}^2 \text{ kh}^{-1}$.

The increasing stack temperature over the operating time leads to an improved ionic conductivity of the electrolyte material. Since its temperature dependency was already studied in detail by the authors, a temperature corrected ASR shift can be calculated according to [5]. The increase of 3.13 K leads to a decrease of the ohmic resistance by $13 \text{ m}\Omega \text{ cm}^2$. Hence, the temperature corrected ASR shift is $30 \text{ m}\Omega \text{ cm}^2 \text{ kh}^{-1}$ and $31 \text{ m}\Omega \text{ cm}^2 \text{ kh}^{-1}$, respectively.

Impedance spectra were recorded every 200 h of operation during the long-term experiment at the operating point. The $-Z(f)$ spectra do not show a significant change within the recorded frequency range indicating a minor effect on the electrodes and their resistances. However, the Nyquist plots in the inset of Figure 5 show that the ohmic resistance increases with

Table 3 Overview of the degradation rates of the respective layers of stack A.

Layer	Voltage at 0 h / V (single cell voltage at 0 h / V)	Voltage at 1,000 h / V (single cell voltage at 1,000 h / V)	Voltage shift / $\text{mV kh}^{-1} \text{ cell}^{-1}$	ASR increase / $\text{m}\Omega \text{ cm}^2 \text{ kh}^{-1} \text{ cell}^{-1}$
1+2	2.686 (1.343)	2.435* (1.218*)	*	*
3+4	2.682 (1.341)	2.698 (1.349)	8	18
5+6	2.657 (1.329)	2.672 (1.336)	8	17
7+8	1.769* (0.885*)	1.751* (0.876*)	*	*
9+10	1.799* (0.900*)	1.793* (0.897*)	*	*

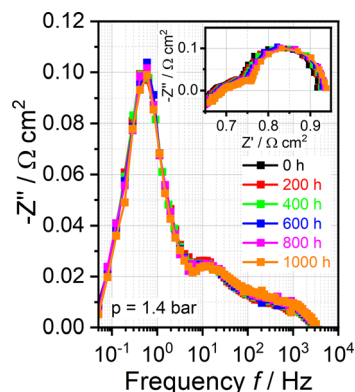


Fig. 5 Impedance data of the 1,000 h experiment conducted at 1.4 bar in steam electrolysis at -0.5 A cm^{-2} with stack A. The data showing the Nyquist plots in the inset is taken from [5].

increasing operating time, as shown within a previous study [5]. The averaged ohmic resistance increased about $18 \text{ m}\Omega \text{ cm}^2$ compared to the begin of the study which is in agreement with the calculated ASR increase shown in Table 3 for the analyzed layers. Hence, it can be concluded that the observed overall degradation of the stack can be mainly ascribed to an increase of the ohmic resistance and the polarization resistances to be affected marginally within this experiment.

3.2 2,000 h Steam Electrolysis Operation at 8 bar

Figure 6 shows the result of the long-term test over 2,000 h at an operating pressure of 8 bar in steam electrolysis mode. The higher pressure leads to higher voltages due to well-known thermodynamic relations. However, activation and diffusion resistances are known to decrease with increasing pressure and could lead to an overall better performance of the stack [32,33]. As already shown by the authors, the studied ESC stack does not show a significant pressure effect since the performance is majorly influenced by the pressure independent ohmic resistance [5,7]. Due to this aspect, the increased pressure led to a higher voltage of the stack and hence to a more significant exothermic operation behavior than the experiment conducted at 1.4 bar. In particular, stack B showed a temperature of 830°C and a voltage of the middle cell of 1.351 V at the beginning of the test. Thus, stack B was operated at a 5 K higher characteristic temperature and a 22 mV higher voltage per cell than stack A.

The voltage shows a nearly linear increase of 31 mV over the first 1,000 h of operation. The ASR increases with $68 \text{ m}\Omega \text{ cm}^2$ during this operating time. Due to the increasing voltage, the characteristic cell temperature increased by 10.4 K. According to the temperature relation of the ohmic resistance presented in [5], the temperature corrected ASR shift is $107 \text{ m}\Omega \text{ cm}^2$. After 1,450 h of steam electrolysis operation, the experiment was conducted in fuel cell mode for 150 h with a gas composition of 75/25 H_2/N_2 at a current

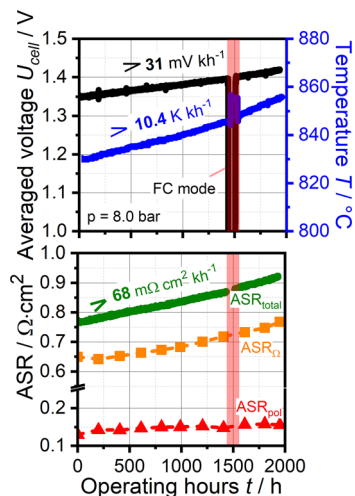


Fig. 6 Constant-current steam electrolysis operation over 2,000 h at 8 bar and 800 °C furnace temperature with stack B. The gas inlet composition was 90% H₂O with 10% H₂. The mass flow on the fuel side was set for a reactant conversion of 70% at a current density of -0.5 A cm^{-2} . Additionally, fuel cell mode was performed over 150 h.

density of 0.21 A cm^{-2} and a RC of 33%. The low current and RC was chosen to operate the stack in the approved temperature range below 860 °C while the same furnace temperature as in steam electrolysis mode (800 °C) could be used. Consequently, the stack showed an averaged cell voltage of 0.867 V and a characteristic temperature of 855.5 °C due to the exothermic fuel cell operation. The fuel cell mode was conducted in order to test the influence of the reversed operation on the stack degradation. Publications showing both a positive and a negative influence of a reversible cycling operation on the long-term performance of a SOEC can be found in literature [15, 21, 34]. In case of an observed superior stability, it was hypothetically achieved due to eliminating the microstructural degradation mechanism that occurs when a high oxygen partial pressure near the oxygen-electrode/electrolyte interface is present [34]. However, a study over 2,000 h with a 30-layer stack conducted at DLR showed the SOFC/SOEC cycling to lead to a higher degradation than during stationary steam electrolysis operation [21]. The authors are aware that whichever the outcome, the experimental conditions within the present study are different since extensive cycling was not performed. The degradation of stack B during the short fuel cell operation was observed to be similar to the electrolysis mode. However, the degradation during the subsequent 450 h of steam electrolysis operation increased significantly with 19 mV (42 mV kh^{-1}), $43 \text{ m}\Omega \text{ cm}^2$ ($95 \text{ m}\Omega \text{ cm}^2 \text{ kh}^{-1}$), and a stack temperature increase of 8 K (18 K kh^{-1}). Consequently, the operation in fuel cell mode turned out to lead to an accelerated degradation within this experiment.

Figure 7a shows the behavior of all layers within this long-term experiment over 2,000 h at 8 bar. Layer 1+2 and 9+10, i.e., the outer layers of the stack, show the highest voltage since their performance is influenced by heat losses towards the lower furnace temperature and the consequently higher resistance of these cells.

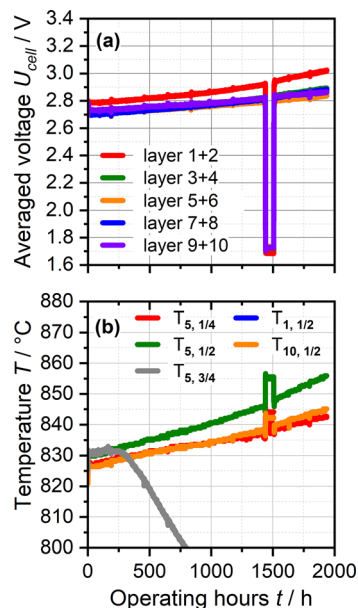


Fig. 7 a) Voltage behavior of the ten layers, and b) measured temperature trend within the stack B over 2,000 h of operation at 8 bar in constant-current steam electrolysis mode.

In particular, layer 1+2 showed an apparently higher voltage over the complete range of operating time. This is in agreement with observations within the 1.4 bar test over 1,000 h where layer 1+2 showed the lowest temperature and accordingly the highest voltage. This phenomenon can most likely be attributed to a slightly lower temperature at the bottom of the furnace environment. At higher pressure the heat losses from the stack box towards the furnace environment become more prominent due to increased convection and lead to an even lower temperature of the bottom cells of the stack. Unfortunately, the sensor of $T_{1,1/2}$ failed already during the heat-up of the stack. Moreover a slight exponential voltage growth of layer 1+2 can be observed whereas the other layers show a more linear characteristic. The measured temperatures plotted in Figure 7b also show a linear increase, though $T_{5,1/2}$ increases with a higher slope than the other temperatures measured within the stack. The thermocouple placed at quarter-length of layer five showed an increase of 15.6 K ($T_{5,1/4}$) and the sensor placed at the middle length of layer ten of 18.1 K over the complete 2,000 h of operation. $T_{5,1/2}$ increased with 25.7 K. Since this thermocouple also showed an offset of 6 K after the long-term test under 95/5 N₂/H₂ forming gas, the slightly increased slope of the measured temperature can be attributed to a drift of $T_{5,1/2}$. However, the impact of the drift ($< 10 \text{ K}$) on the calculated ASR is rather small. By taking $T_{10,1/2}$ for the ASR calculation the resistance would solely increase $6 \text{ m}\Omega \text{ cm}^2$ less.

Table 4 gives an overview of the voltage and ASR shifts of stack B. Note that the voltage and ASR shift rates are shown in the specific unit per cell for the first kh.

The average voltage shift per cell was 33 mV kh^{-1} , and the ASR per cell increased by $72 \text{ m}\Omega \text{ cm}^2 \text{ kh}^{-1}$ over the first

Table 4 Overview of the degradation rates of the ten layers of stack B.

Cell layer	Voltage at 0 h / V (single cell voltage at 0 h / V)	Voltage at 1,000 h / V (single cell voltage at 1,000 h / V)	Voltage shift / mV kh ⁻¹ cell ⁻¹	ASR increase / mΩ cm ² kh ⁻¹ cell ⁻¹
1+2	2.788 (1.394)	2.864 (1.432)	38	82
3+4	2.703 (1.352)	2.780 (1.390)	39	82
5+6	2.701 (1.351)	2.763 (1.382)	31	68
7+8	2.701 (1.351)	2.772 (1.386)	36	77
9+10	2.739 (1.370)	2.786 (1.393)	24	53

1,000 h. The average temperature corrected ASR shift is 101 mΩ cm² kh⁻¹. Consequently, the experiment conducted at 8 bar showed both in voltage and ASR an almost four times higher degradation than at 1.4 bar. The authors are aware that this has no statistical significance, but both experiments conducted at 1.4 and 8 bar indicate a significant impact of the operating pressure on the long-term stability. Furthermore, after the operation in fuel cell mode the average voltage shift for the remaining 450 h in electrolysis mode was 26 mV per cell (58 mV kh⁻¹) and the ASR per cell increased by 55 mΩ cm² (122 mΩ cm² kh⁻¹). Hence, it can be concluded that the fuel cell mode had a significantly worsening effect on the performance stability of the stack since the degradation accelerated by almost 60%. One possible explanation for the higher degradation might be the increased transversal and longitudinal temperature gradients within the stack during the highly exothermic fuel cell operation. These temperature gradients cause thermomechanical stress within the cell structure and might lead to contact losses of the fuel or the air electrode from the electrolyte [35,36]. The weakened contact at the electrode/electrolyte interface could consequently lead to extended contact losses in the subsequent full loaded electrolysis operation and increased ohmic resistances.

Impedance spectra were recorded every 200 h of operation during the long-term experiment at -0.5 A cm⁻².

The -Z(f) diagram in Figure 8 shows the visible peaks at approximately 10 and 1,500 Hz to shift towards higher values on the imaginary axis with increasing operating time. Though the peaks in a -Z(f) diagram generally do not fully describe resistances, higher imaginary values nevertheless indicate increasing resistances. In particular, the processes around 10³ Hz and 10¹ Hz can be attributed to the air electrode and fuel electrode of the ESC stack, respectively [7]. Consequently, both electrodes show a considerable performance loss during the experiment. However, the Nyquist plots in the inset of Figure 8 show that the increased electrode resistances play a subordinate role compared to the predominant change of the ohmic resistance. The primarily increased ohmic resistance could be attributed to Nickel depletion and the consequently longer O²⁻ pathway as it was already described in literature [14, 27, 37, 38] (see Section 3.5.2).

3.3 Co-electrolysis over 1,000 h

Figure 9 shows the result of the long-term test over 1,000 h at operating pressures of 1.4 and 8 bar in steam and co-electrolysis mode. During the first 160 h of operation, steam electrolysis at 1.4 bar was conducted in order to enhance the comparability with the test of stack A. An averaged voltage increase of 3 mV for the layer 5+6 was observed for stack C. This is in good agreement with the experiment of stack A where a voltage increase of 2 mV was measured during the first 160 h.

The authors are aware that this short period of testing in steam electrolysis mode at 1.4 bar does not allow a profound forecast of the degradation over 1,000 h. However, it strongly indicates that the long-term stability of the ESC stacks A and C in steam electrolysis is similar and the recorded data is valid.

After the 160 h of steam electrolysis, co-electrolysis operation at 1.4 bar was conducted for 500 h. Due to the operation with CO₂ in the feed gas and the additional occurrence of the endothermic reverse water-gas shift (rWGS) reaction, the stack operating temperature was significantly lower which subse-

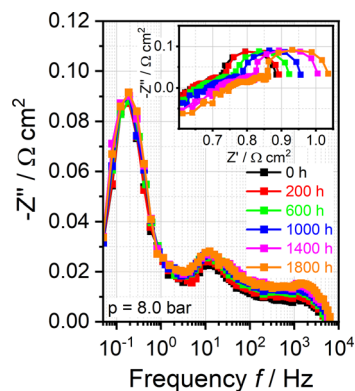
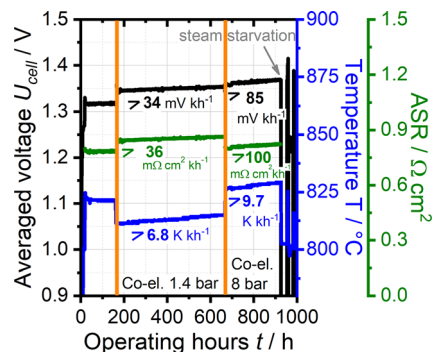


Fig. 8 Impedance data of the 2,000 h steam electrolysis experiment conducted at 8 bar with stack B.


 Fig. 9 Constant-current operation in steam and co-electrolysis mode over 1,000 h at 1.4 bar and 8 bar with stack C. The gas inlet composition was 90/10 (H₂O/H₂) in case of steam electrolysis and 63.7/31.3/3.3/1.7 (H₂O/CO₂/H₂/CO) during co-electrolysis operation. The mass flow on the fuel side was set for a constant reactant conversion of 70% at a current density of -0.5 A cm⁻².

quently led to a higher voltage. An accelerated degradation was observed during this operational regime. The voltage increased by 17 mV which corresponds to a voltage shift rate of 34 mV kh^{-1} and an increase of the ASR of $36 \text{ m}\Omega \text{ cm}^2 \text{ kh}^{-1}$. Due to the increasing voltage the temperature increased by 3.4 K (6.8 K kh^{-1}). The temperature corrected ASR can be calculated to $68 \text{ m}\Omega \text{ cm}^2 \text{ kh}^{-1}$. Compared to steam electrolysis operation conducted at the same pressure with stack A, the performance loss during co-electrolysis mode almost doubled.

Figure 9 shows that the co-electrolysis operation at an elevated pressure of 8 bar led to an even more significant degradation than at 1.4 bar. During the 260 h of operation, the voltage increased by 85 mV kh^{-1} and the ASR by $100 \text{ m}\Omega \text{ cm}^2 \text{ kh}^{-1}$. This implies an approximately three times higher degradation compared to the low pressure operation.

Figure 10a shows the behavior of the stack layers within this long-term experiment over 1,000 h. Layer 1+2 and 9+10, i.e., the outer layers of the stack, showed the highest voltage since their performance is majorly influenced by the heat losses towards the lower furnace temperature and the consequently higher resistances of these cells. It can be seen, that the operation at the higher voltage led to a significantly increased degradation within this study.

Furthermore, a comparison between the recorded temperatures at 1.4 and 8 bar showed the stack temperature gradients to increase significantly at higher pressure. This phenomenon is caused by (i) an increase of internal heat production due to the increased extent of exothermic methanation reaction, and (ii) caused by increased heat losses of the stack towards the lower furnace temperature due to a higher ΔT and the increase of convection at higher operating pressure. As can be seen in Figure 10, the thermocouples $T_{1,1/2}$ measuring close to the bottom and $T_{10,1/2}$ measuring close to the top of the stack

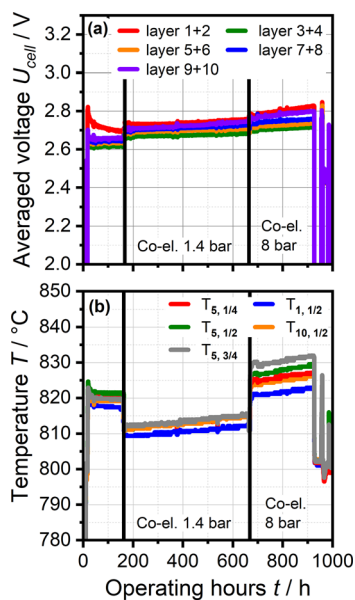


Fig. 10 a) Voltage behavior of the ten layers, and b) measured temperature trend within the stack over 1,000 h at both 1.4 and 8 bar in constant-current steam and co-electrolysis mode.

show the lowest temperature. In contrary, at three-quarter length of layer 5 ($T_{5,3/4}$) the highest temperature and probably the hotspot within these experimental conditions was observed. The location of this hotspot is in good agreement with a thermal 3D simulation of the stack in exothermic fuel cell mode [25].

During the co-electrolysis operation at both 1.4 and 8 bar, the outlet gas composition of the stack was monitored *via* a gas analyzer and showed the molar fractions to follow the thermodynamic equilibrium. This behavior has already been shown within detailed co-electrolysis studies by the authors [7, 29, 39].

At 930 h, a malfunction of the water pump for the steam supply occurred and the automated safety procedures of the test rig triggered a load shedding. Figure 11 shows the behavior of the voltages and the simultaneously recorded analysis of the outlet gas composition in detail. Note that the molar fraction of H_2O is not analyzed since H_2O is removed from the gas mixture upstream of the analyzer.

The malfunction of the water pump led to steam starvation and in turn to a voltage increase as well as a voltage fluctuation of almost 20 mV per cell. In particular, the outer layers of the stack showed the most significant influence and voltage increase since their temperature was lowest during operation. The authors assume a small gas bubble entered and remained in one piston of the liquid water pump of the test rig and considerably decreased the mass flow for evaporation. The gas analysis in Figure 11b shows the outlet gas composition during this time period with decreasing fractions of CO_2 and H_2 and increasing fractions of CO and CH_4 , respectively. Based on the gas analysis, a decrease of the steam supply by almost 40% could be calculated which led to a RC of 94% within the stack. Due to this high conversion, the H_2O fraction decreases to a minimum within this scenario while a higher amount of CO_2 is shifted towards CO by the rWGS reaction and simultaneously a higher extent of electrochemical CO_2 reduction

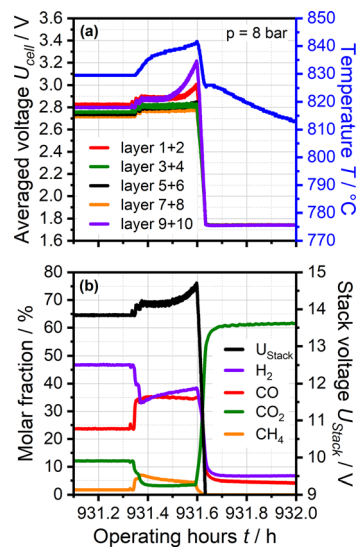


Fig. 11 a) Characteristic stack temperature depicted with the voltage behavior of the ten layers; b) recorded analysis of the outlet gas composition during the operating time of the water pump's malfunction.

occurs. Hence, the increased amount of produced CO could be consumed by a higher extent of the exothermic methanation reaction which led to the observed increased stack temperature. By calculating the thermodynamic equilibrium with the reduced H₂O supply and the accordingly high conversion, a H₂/CO ratio of approximately 1.5 can be found for this scenario. A reduction of 40% of the steam supply in combination with the related high conversion of >90% leads to approximately 5% of solid carbon formation according to the thermodynamic equilibrium at these experimental conditions. The thermodynamic equilibrium was calculated with the software of the Glenn Research Center [40]. Since the outer layers of the stack showed the lowest temperature due to the heat losses towards the furnace environment, the risk and amount of solid carbon deposition increases. Additionally, a slightly unequal distribution of reactants between the different stack layers could lead to the observed more significant voltage increase of the outer layers.

When steam starvation occurred, the characteristic temperature of the stack increased due to the considerable rise of the RC and the higher extent of methanation. The increased temperature led to a higher H₂ concentration due to thermodynamic relations and intensified the voltage increase until the automated safety procedure of the test rig intervened. After this event a continuation of operation was attempted twice but was impeded since the stack exceeded the maximum voltage. Most likely the high RC and carbon deposition irreversibly damaged the cell structure since the ohmic resistance showed a considerable increase after the steam starvation event (see Figure 12).

During the operation of stack C in steam and co-electrolysis mode, impedance spectra were recorded in the same manner as conducted with stack A and B in order to quantify the influence of the operating mode on the performance loss in more detail. Figure 12 shows the measured ohmic resistance, the temperature dependent ohmic resistance of one layer according to [5], the calculated polarization resistance and the characteristic stack temperature during the 1,000 h test. Note that the measured ohmic resistance shown in the graph is an aver-

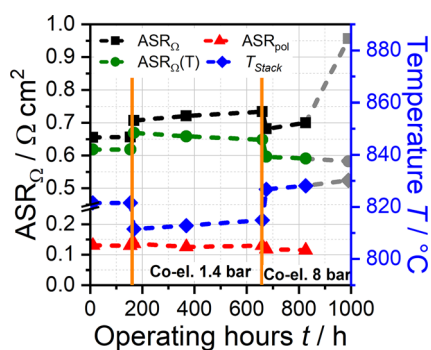


Fig. 12 Measured ohmic resistance (ASR_{Ω}), temperature-dependent ohmic resistance according to [5] ($ASR_{\Omega}(T)$) and measured characteristic stack temperature (T_{Stack}) during the steam and co-electrolysis experiment at 1.4 and 8 bar.

age of the cell layers 5+6 since the depicted characteristic stack temperature is measured on layer 5.

EIS was performed before and after the operation in pure steam electrolysis mode at 1.4 bar. A significant increase neither of the voltage nor of the ohmic resistance was observed. This is in good agreement with the results of the pure steam electrolysis mode performed with stack A, where a minor degradation over 1,000 h at the same operating condition was observed (see Figure 3). The measured ASR_{Ω} was $0.655 \Omega \text{ cm}^2$ at a characteristic stack temperature of 821.5°C at the beginning of the test. After 160 h the measured ASR_{Ω} was $0.657 \Omega \text{ cm}^2$ and thus showed an insignificant increase over the operating time. A small deviation of the measured ohmic resistance under load and the temperature-dependent resistance according to [5] ($ASR_{\Omega}(T)$) can be seen. However, it solely accounts for $16 \text{ m}\Omega \text{ cm}^2$. The small deviation can be explained by the fact that the resistance at the inlet and the outlet of the stack is highly influenced by heat losses towards the lower furnace temperature in exothermic operating mode which leads to slightly higher averaged resistances recorded by EIS.

The measurements during the co-electrolysis operation at 1.4 bar show the ohmic resistance and the temperature to increase simultaneously. The deviation between the measured ASR_{Ω} and the $ASR_{\Omega}(T)$ becomes more significant, due to the more dominant degradation of the stack. As can be seen in the graph, the performance loss increases at 8 bar since the slope of the measured ohmic resistance increases. After the incident of steam starvation at 930 h of operation the ohmic resistance showed a major increase which led to the abortion of the test.

3.4 Comparison of the Experiments

In order to compare the results obtained from the experiments with stack A–C, Figure 13 shows the degradation based on the increase of the measured ohmic resistance. All conducted experiments showed the performance loss to be majorly caused by an increase of the ohmic part in the EIS spectra. Stack A and the first 160 h of stack C were operated at

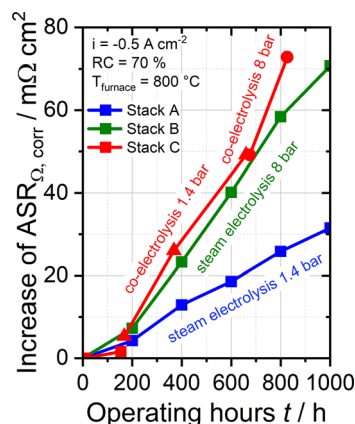


Fig. 13 Increase of the ohmic resistance during the conducted experiments in steam and co-electrolysis with stack A–C.

the same condition in steam electrolysis mode and show a comparable increase of the measured ASR_{Ω} . Stack B which was operated in steam electrolysis at 8 bar and thus at a higher voltage and temperature showed an apparently more significant increase of the ohmic resistance. Compared to the operation of stack A at 1.4 bar, the rise of the ohmic resistance of stack B almost doubled after 1,000 h. The co-electrolysis operation at 1.4 bar with stack C showed a considerable increase of the ohmic resistance. Furthermore, the operation at the elevated pressure of 8 bar led to an even more significant increase of the resistance.

Table 5 summarizes the conducted experiments with the averaged voltage of the middle cell, the averaged characteristic stack temperature and the corresponding increase of the total and ohmic resistances over the operating time. Note that all resistances are normalized or extrapolated to 1 kh. The ASR is additionally shown with the specific temperature correction according to the discussion of the related experiments. As shown before, the polarization resistances are in similar ranges to each other and play a subordinate role compared to the ohmic resistance increase. Hence, the polarization resistances are not considered here. Stack A showed a voltage shift of 8 mV over the 1000 h of testing at 1.4 bar and a RC of 70% at -0.5 A cm^{-2} . Experiments in atmospheric conditions with a similar ESC single cell configuration have already shown a voltage shift of approximately 7 mV kh^{-1} at current densities between -0.5 and -0.9 A cm^{-2} [13, 41]. Both the steam content (75%) and the reactant conversion (51%) were lower than the ones of the presented study whereas the temperature was slightly higher ($\sim 850 \text{ }^{\circ}\text{C}$). The electrolyte material of the cell

was 6Sc1CeSZ which has a generally higher conductivity than the 3YSZ material used in the stacks of the current study, hence higher current densities could be achieved while operating in long-term endothermic mode [30]. The same ESC architecture with a 3YSZ electrolyte on single cell level was used in another long-term study at atmospheric conditions [15]. A voltage shift of 5 mV kh^{-1} was shown for a current density of -0.7 A cm^{-2} and 60% conversion which corresponded to a temperature corrected ASR increase of $7 \text{ m}\Omega \text{ cm}^2$. Both ESC single cell studies also observed a predominant increase of the ohmic contribution and only a minor contribution from the electrodes during the operation which is in agreement with the findings of the current study. One major difference between the single cell and stack experiments is the additional contribution of contact resistances (i.e., bipolar plates) to the overall measured ohmic resistance of a stack [5]. Since these resistances additionally increase during the operation time, long-term stack experiments tend to show higher performance losses [19]. Furthermore, temperature gradients, current density-, gas-, and conversion distribution can highly differ from single cell to stack experiments. Moreover, the impacts of piping and seals can lead to further degradation contributions to stacks [19, 42].

On stack level, the long-term behavior was mainly investigated on stacks with cathode supported cells (CSC) at atmospheric operating pressures [16–18, 20, 43, 44]. Fang et al. investigated a two-layer stack (Ni8YSZ/8YSZ/LSCF) over more than 10,000 h of steady state electrolysis operation at $800 \text{ }^{\circ}\text{C}$ and observed a voltage shift of approximately $4\text{--}5 \text{ mV kh}^{-1}$. The stack was operated in endothermic mode

Table 5 Overview of the experimental conditions of the conducted studies with the three stacks A–C. The averaged voltage of the middle cell, the averaged characteristic stack temperature and the increase of the total and ohmic resistances are given per kh.

	Stack A	Stack B	Stack C	Stack C	Stack C
Operating mode	H ₂ O-electrolysis	H ₂ O-electrolysis	H ₂ O-electrolysis	Co-electrolysis	Co-electrolysis
Time / h	1,000	2,000	160	500	260
Pressure / bar	1.4	8	1.4	1.4	8
Stack temperature at start / °C	825.3	830.2	823.1	811.5	827
Stack temperature increase / K	3.13	10.4	2.4	6.8	9.7
Voltage at start / V	1.329	1.351	1.325	1.35	1.369
Voltage increase / mV	8	31	12	34	85
p _{H₂O} / bar	1.26	7.2	1.26	0.89	5.10
p _{H₂} / bar	0.14	0.8	0.14	0.05	0.27
p _{CO₂} / bar	–	–	–	0.44	2.50
p _{CO} / bar	–	–	–	0.02	0.13
ASR _{total} at start / mΩ cm ²	808	767	797	843	804
ASR _{total} increase / mΩ cm ² kh ⁻¹	18	68	15	36	100
ASR _{total} increase with temperature correction / mΩ cm ² kh ⁻¹	32	107	26	68	137
ASR _Ω increase / mΩ cm ² kh ⁻¹	18	32	12	56	72
ASR _Ω increase with temperature correction / mΩ cm ² kh ⁻¹	32	71	23	88	109 (157 if incident considered)

and with 50% of H₂O content at -0.5 A cm^{-2} . Lang et al. investigated a 30 layer stack at atmospheric pressure with identical cells as used within the current study and observed a voltage shift of approximately 6 mV kh^{-1} and a ASR shift of approximately $13 \text{ m}\Omega \text{ cm}^2$ (without temperature correction) during steady state electrolysis operation at -0.5 A cm^{-2} and a conversion of 70% [21]. The stack temperature increased with about 3 K kh^{-1} which leads to an temperature corrected ASR shift of approximately $26 \text{ m}\Omega \text{ cm}^2$ by assuming the temperature dependency of the stack measured by the authors [5]. The cell voltages and the inlet gas composition were similar to the current study. Latest published results of a 30 layer ESC stack test showed an ASR shift of $13 \text{ m}\Omega \text{ cm}^2$ (with temperature correction) for thermoneutral operation at ambient pressure [45]. However, the stack design was slightly improved compared to the one used within the current study. Consequently, the observed degradation of stack A is in a similar range to relevant stack investigations at ambient pressure, though it shows slightly higher voltage and ASR shifts. Furthermore, both the CSC and the ESC investigations showed that the ohmic resistance predominantly increased [20,21].

The number of publications related to long-term stack performances under pressurized operation is limited due to the limited presence of pressurized stack test rigs. Jensen et al. investigated an 11-cell CSC stack at elevated operating pressure of 10 bar over a duration of 200 h in steady state steam electrolysis [22]. The applied current density was in a range between -0.18 and -0.25 A cm^{-2} . The voltage shift was found to be around $90\text{--}270 \text{ mV kh}^{-1}$ though several incidents during the operation raised uncertainties about the meaningfulness of the achieved results. In comparison, a similar stack tested at ambient pressure condition and higher temperature led to a voltage shift of 40 mV kh^{-1} [46]. Despite the uncertainties, these results might also indicate higher stack degradation at higher operating pressures. Stack B of the current study showed a voltage shift of 31 mV kh^{-1} and a temperature corrected ASR shift of $107 \text{ m}\Omega \text{ cm}^{-2}$ at 8 bar. However, both the voltage and ASR shift are approximately four times higher than during the experiment conducted with stack A at 1.4 bar.

The co-electrolysis experiment conducted with stack C at 1.4 bar showed a noticeably higher degradation than stack A. This indicates a negative influence of the used CO₂ or CO on the long-term performance. A higher degradation during co-electrolysis operation was already observed within single cell and stack tests and was ascribed to additional contaminants like sulfur which can be brought in by the carbonaceous gas leading to an inactivation of the catalyst [46–48]. Schäfer et al. showed a degradation of $19 \text{ m}\Omega \text{ cm}^2 \text{ kh}^{-1}$ with a four layer CSC stack under co-electrolysis conditions at ambient pressure and -0.5 A cm^{-2} . In comparison, stack C of the current study showed a higher ASR shift ($36 \text{ m}\Omega \text{ cm}^2 \text{ kh}^{-1}$; $68 \text{ m}\Omega \text{ cm}^2 \text{ kh}^{-1}$ with temperature correction) whereas it was operated at a significantly higher voltage. The increase of the operating pressure up to 8 bar caused an additional increase of the degradation of stack C, which is in agreement with the comparison of the results of stack A and B.

3.5 Post-test Analysis (PTA)

All stacks were disassembled after the long-term experiments in order to examine the influence of the different operating conditions on the stack components and cell microstructure. Samples from the inlet, middle and outlet of layer five of each stack including the bipolar plate (BPP) was embedded in resin for cross-section preparation and investigations *via* SEM and EDX while the rest of the stacks were inspected visually.

3.5.1 Investigation of the Bipolar Plates

Within stack A and B no cell cracks or traces of burning on either the anode or the cathode side were observed. This is in good agreement with the recorded data since prominent increases in temperature were not measured during both experiments. Figure 14 shows the cross section of the two BPPs close to the air outlet of stack A and B. The pictures show the steel of the BPP (upper part in light gray), the marked oxide layer and the porous contact paste towards the air electrode underneath. Generally, a growing oxide layer at the BPP leads to an increasing ohmic resistance of the specific repeating unit and of the whole stack.

A different extent of oxide layer formation and a chromium accumulation at the interface was found within the analysis. The oxide layer at the BPP of stack B was almost twice as thick as the one of stack A. This can most likely be attributed to the doubled operating time of stack B since an oxide layer growth in Ni-Cr steel generally follows a parabolic time law in the temperature range of $750\text{--}950 \text{ }^\circ\text{C}$ [49]. Consequently, the significantly higher partial pressure of oxygen within the experiment of stack B plays a subordinate role for the oxide layer growth at the BPP. Furthermore a loss of contact between the oxide layer and the contact paste of stack B was observed.

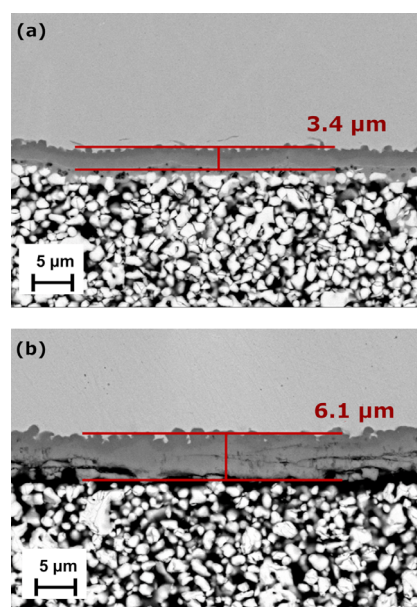


Fig. 14 Cross section of the bipolar plates close to the air outlet with the formed oxide layers.

However, the related experimental results of stack B do not lead to the expectation that this loss of contact happened during operation since the compression weight on top of the stack effectively presses on these contact spots between BPP and air electrode. It is assumed that the slight delamination consequently occurred during the stack disassembly and sample preparation. Within the PTA cross sections of the BPP at the air inlet and at the middle length were prepared and investigated *via* SEM but did not show different results than the one shown in Figure 14. The significant difference in ohmic resistance between stack A and B hence did not originate from the oxide layer formation at the investigated BPPs.

3.5.2 Investigation of the Electrodes

Figure 15 shows the cross section of the fuel electrode (Ni-GDC) and partly of the electrolyte (3YSZ) of stack A and B. The samples were taken close to the inlet of the stacks. Ni coarsening and depletion is conspicuous in the fuel electrode of stack B and a comparably denser layer of Nickel on the surface of the electrode was observed. These observations were particularly made at the inlet of the stack whereas significantly less Ni depletion was observed towards the stack outlet. This observation is in agreement with other studies related to long-term SOEC investigations [17, 50]. Since the partial pressure of H₂O is highest at the inlet, this observation indicates a direct correlation between steam content and Ni depletion. Though stack B was operated over a longer operating time, it is unlikely that a high amount of Ni depletion and accumulation on the surface considerably occurs only within the second half of the 2,000 h test.

In literature a direct correlation between the partial pressure of H₂O and Ni mobility and depletion was already dis-

cussed for steam electrolysis operation, though no mechanism has been proven so far [10, 11, 27, 51–55]. However, the studies mostly focus on fuel electrode supported single cells with Ni-YSZ electrodes. Furthermore, the cells were operated at a significantly higher current density leading to high overpotential and temperature gradients perpendicular to the electrode/electrolyte interface. It is hypothesized that these gradients are the driving force for the loss of contact between Ni and YSZ and the related depletion of Ni *via* volatile Ni(OH)_x species [10, 17, 27, 51, 55–57]. However, in the present study a composite electrode of Ni-GDC in an electrolyte supported cell was used in the stacks. Ni-GDC is a wellknown mixed ionic and electron conducting material which can offer a significantly broader triplephase boundary (TPB) and reaction region than Ni-YSZ material. Consequently, all potential and temperature gradients within the porous electrode decrease and should lead to less Ni evaporation [11, 56]. In the present study the operating voltage of the middle cell of stack B was 22 mV higher than the one of stack A at the beginning of the tests. Furthermore, the temperature difference between both stacks was approximately 5 K whereas the reactant conversion of 70% was constant. Hence, the difference of the potential and temperature gradients of stack A and B were marginal and cannot be responsible for the apparently higher Ni depletion in stack B. However, the partial pressure of H₂O at the inlet of stack A was 1.26 bar (H₂ 0.14 bar) whereas it was 7.2 bar (H₂ 0.8 bar) during the operation of stack B. The molar fraction of Ni(OH)₂ as the predominantly occurring hydroxide species was calculated based on thermodynamic equilibrium to 9·10⁻¹¹ by using the experimental conditions for stack A and the averaged gas composition. The equilibrium was calculated with FactSage software [58]. The calculation of the thermodynamic equilibrium shows a linear dependency of the partial pressure of Ni(OH)₂ with the operating pressure. The high partial pressures of H₂O and H₂ in stack B can consequently lead to a significantly higher Ni mobility *via* a high partial pressure of the hydroxide species. Additionally, the decreased diffusion resistance during pressurized operation and the high reactant conversion of 70% might contribute to an increased Ni(OH)_x output and depletion rate. However, it is difficult to assess how operating parameters influence the formation and the diffusive characteristic of Ni(OH)_x species during pressurized operation, due to insufficient knowledge of the underlying mechanisms [10, 11, 17, 52]. But as a consequence, the loss of Ni in the porous electrode structure leads to an increased ohmic resistance since the ionic conduction pathway of the O²⁻ ions becomes longer. This correlation was already shown by publications where the long-term behavior of Ni-YSZ fuel electrodes was investigated [37, 59–61]. Though GDC with its electro-catalytic characteristic is present in the used electrodes, the ohmic resistance might increase since the electrical conductivity of GDC is lower than the one of Ni [5, 62]. Furthermore, the electrical contact between the GDC particles within the porous electrode could become worse, due to the loss of highly conductive Ni material and relatedly formed cavities. Hence, the predominant electrochemical reaction zone moves

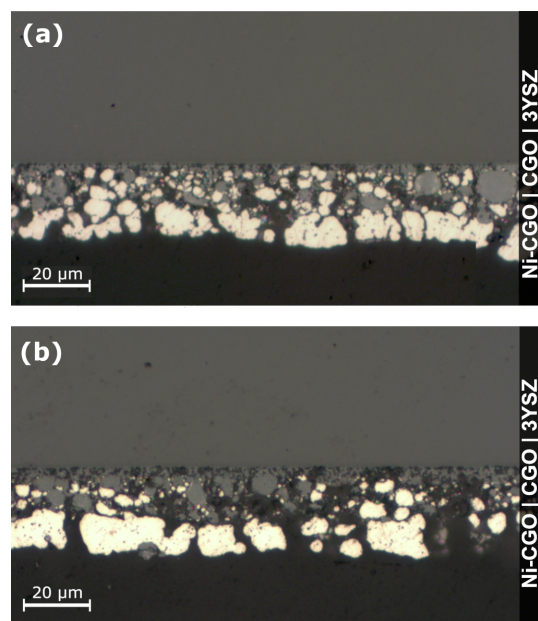


Fig. 15 Cross section showing the fuel electrode and electrolyte of stack A and B.

to the outer part of the electrode layer [30,63]. Additionally, the loss of Ni leads to an increased polarization resistance of the fuel electrode which is in good agreement with the experimental results shown in the EIS spectra of Figure 8. However, the magnitude of the increase in ohmic and polarization resistance might be lower than it would be for Ni-YSZ electrodes, since ions and electrons can be distributed *via* the GDC material and can still participate in the electrochemical reaction.

Within the fuel electrodes of both stacks traces of silicon contamination were observed *via* EDX. The possible major origin of this contaminant is both the liquid water for evaporation and the glass sealants of the stack. Silicon in the form of silicon dioxide is known to be solved in liquid water and very difficult to remove. Though ultrapure water was used for the experiments, a concentration of 4 to 7 $\mu\text{g L}^{-1}$ was measured in several analyses of the liquid phase at DLR. The contamination was observed to be highest close to the inlet of the cells, whereas significantly less silicon was found at the outlet of the cells. Figure 16 a and b show representative EDX images of the stacks A and B at the inlet of the cells where the maximum concentration of silicon was observed. In case of stack A, an averaged silicon contamination of approximately 2.3 mass-% was found across the fuel electrode thickness at the inlet whereas spots with a maximal concentration of 5.5 mass-% were found close to the Ni/CGO-CGO interface (Figure 16 a spots 9, 10). In contrast, spots with a maximum silicon contamination of 0.9 mass-% were found close to the outlet of the cell.

The maximum silicon contamination of stack B was found with 13.4 mass-% at the inlet close to the Ni/CGO-CGO interface (Figure 16 b spots 8, 9), whereas a maximum silicon contamination of 1.4 mass-% was found at the outlet of the cell. Please note that the EDX analysis is used for a qualitative comparison between stack A and B and showed that stack B was significantly more contaminated with silicon than stack A. This observation can be attributed to the doubled operating

time and most likely to the higher partial pressure of silicon within the electrode compartment during operation. However, the low degradation of stack A is promising although the cells were contaminated with silicon. To quantify the impact of silicon contamination on the actual degradation rate of a stack has to be subject of further investigations.

A partial delamination of the air electrode from the electrode/electrolyte interface was observed for stack B. This phenomenon could significantly contribute to the predominant increase of the ohmic resistance during the experiment. In particular the partial delamination was observed close to the outlet, i.e., within the cell area with the highest partial pressure of oxygen (p_{O_2}) during operation. It cannot be fully clarified if this delamination happened during or after the operation or during the disassembly of the stack. Unfortunately, a preparation of a cross-sectional sample of a spot close to the outlet of the cell was not possible due to the instability of the cell during the disassembly. However, since it was not observed at the inlet or middle length of the cell there is a strong indication that it happened already during operation. In accordance with the experimental conditions, the p_{O_2} of stack B was 2.9 bar at the outlet. In literature the delamination of the air electrode was extensively investigated for electrolysis operation with LSM electrodes and was mostly assigned to the high p_{O_2} at the interface or the formation of a secondary phase [64–66]. The latter was not observed within the PTA of stack B for the samples prepared of the inlet or the middle length of the cell. The high p_{O_2} within the air electrode compartment and at the electrode/electrolyte interface might have led to a weakening of the interface between YSZ and the GDC barrier layer and consequently to the observed delamination [67].

Stack C which was mostly operated in co-electrolysis mode at 1.4 and 8 bar showed an apparent delamination of the fuel electrode from the electrolyte, as can be seen in Figure 17. The experiment was aborted, due to steam starvation accompanied by a reactant conversion >90%. After the incident the stack showed a significantly higher ohmic resistance which could be caused by the observed delamination of the fuel electrode.

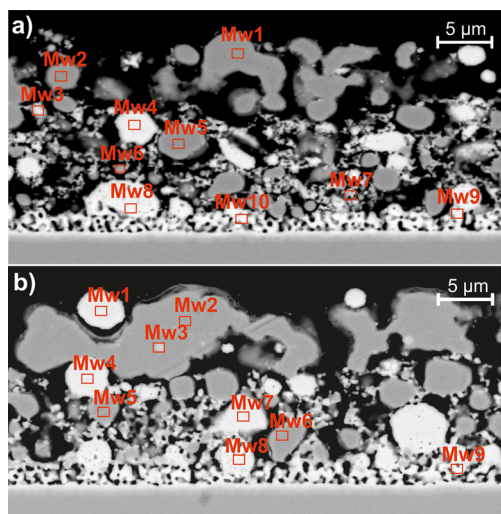


Fig. 16 Representative cross-section of the Ni-CGO fuel electrode from a spot close to the inlet of the middle cell of a) stack A; and b) stack B for a qualitative comparison of the silicon contamination *via* EDX.

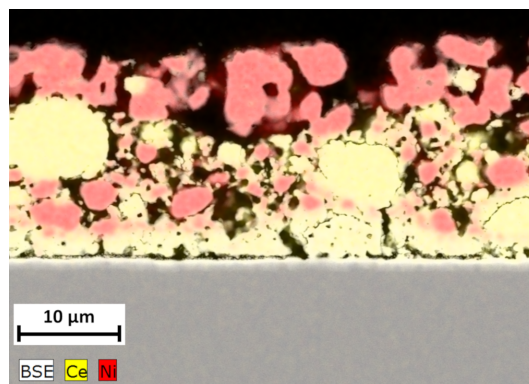


Fig. 17 Backscattered electrons image of the fuel side of cell 5 of stack C. Ceria (Ce) is marked in yellow, Ni in red.

As mentioned within Section 3.3, it is expected that solid carbon formed close to the electrode/electrolyte interface where the lowest H/C ratio is present during the operation at high conversion rates. Furthermore, the solid carbon could have been oxidized when the current decreased and enough steam or CO₂ was present due to a lower reactant conversion. Both, the reduction and oxidizing process are associated with a volume change within the microstructure of the electrode which can lead to a damage of the electrode structure and consequently to the observed delamination. However, if the delamination of the fuel electrode already began before the incident of steam starvation could not be fully clarified within the PTA. Furthermore, thermomechanical stress might have contributed to the structural defect since the stack temperature dropped by approximately 15 K within 1 minute after load shedding (see Figure 11 a).

Electroreduction of the 3YSZ electrolyte and related conduction loss due to high reactant conversion can generally lead to significantly increased ohmic resistances. However, since the cell voltage (except layer 9+10) stayed below 1.5 V during the steam starvation incident, it can be assumed that the electrolyte itself was not irreversibly damaged within the current study [68].

Nickel depletion was observed at the fuel electrode, though to a much lesser extent than observed in stack B (see Figure 17). The lower depletion can be attributed to the shorter operating time under elevated pressure and the lower partial pressure of H₂O at the inlet during the co-electrolysis mode. However, the ohmic resistance of stack C showed a significantly higher increase at 1.4 bar than during the steam electrolysis operation of stack A. Experimental data about the long-term behavior during co-electrolysis operation can be found in literature [69–71]. Compared to steam electrolysis, the operation with CO₂ in the inlet led to increased degradation rates in all studies. The higher performance loss was mostly ascribed to the adsorption of impurities like sulfur at active sites. Partly inactivation of the electrode with that respective contaminant leads to locally increased current densities, higher overpotentials and hence a decreased long-term performance. Contamination with silicon was also observed for stack C but qualitatively compared slightly less than within the PTA of stack A. More specifically, an averaged contamination of 2.9 mass-% across the fuel electrode thickness at the inlet with a maximum contamination of 4.3 mass-% close to the Ni/CGO-CGO interface was found. This could be attributed to the lower steam content during the co-electrolysis operation. Except for the fuel electrode delamination, no suspicious observations of the stack and/or cell microstructure were made.

4 Conclusion

In this study three identically constructed ten-layer stacks (A–C) with electrolyte supported cells were tested in exothermic steam and co-electrolysis mode at elevated pressures of 1.4 and 8 bar. Investigations during constant-current operation

at a current density of -0.5 A cm^{-2} and a reactant conversion of 70% were carried out over 1,000–2,000 h. The inlet gas molar fractions for steam electrolysis was 90/10 (H₂O/H₂) and 63.7/31.3/3.3/1.7 (H₂O/CO₂/H₂/CO) for co-electrolysis operation.

All stacks showed highly similar resistances according to their respective temperature dependency at the beginning of the tests, indicating a high level of accuracy and repeatability during manufacturing. Stack A was operated in steam electrolysis mode at 1.4 bar over 1,000 h and showed a low degradation of 8 mV kh^{-1} per cell and an ASR shift of $18 \text{ m}\Omega \text{ cm}^2 \text{ kh}^{-1}$ per cell. The main reason for the observed performance loss could be ascribed to the time-dependent increase of the ohmic resistance whereas the polarization resistances remained almost constant.

Stack B was operated at 8 bar over 2,000 h and showed an almost four times higher voltage and ASR shift than stack A. Impedance analysis showed increased resistances for both the air electrode and the fuel electrode. However, the major part of the observed degradation could be attributed to the ohmic resistance. A short period of fuel cell operation of about 150 h was also performed with stack B in the second half of the testing time. The degradation became noticeably higher during the subsequent constant steam electrolysis operation. Within the post-test analysis of the two stacks (A and B), a significantly higher extent of Ni depletion in the fuel electrode was observed for stack B. This phenomenon indicates that the operating pressure has a considerable influence on the nickel mobility and could lead to a decrease in the effective conductivity of the fuel electrode. Furthermore, a partial delamination of the air electrode was observed particularly at the outlet of the stack. However, delamination attributed to high partial pressure of oxygen at the outlet cannot be confidently confirmed, since delamination is also possible to occur during the disassembly of the stack.

Stack C was operated in steam electrolysis mode for the first 160 h and showed a highly similar degradation as stack A. Afterwards, the stack was operated in co-electrolysis mode for 500 h at 1.4 bar. The performance loss increased noticeably and the ohmic resistance was identified again to be the dominant cause of the degradation. The voltage shifted by 34 mV kh^{-1} and the ASR by $36 \text{ m}\Omega \text{ cm}^2 \text{ kh}^{-1}$. The stack was operated for another 260 h (930 h total operating time) in co-electrolysis mode at 8 bar until it unfortunately failed due to a short steam starvation incident. After this event a continuation of operation was attempted twice but was impeded since the stack exceeded the maximum voltage due to a highly increased ohmic resistance. Within the PTA a delamination of the fuel electrode was observed which might be attributable to formed and reoxidized solid carbon within the microstructure of the electrode and thus a weakening of the mechanical property due to volume changes within the substrate.

Finally, the authors would like to point out that the conducted experiments indicate that a higher degradation is associated with the higher operating pressure, but a general statement about the long-term stability is truly not possible at this time. The authors are aware that neither 1,000 nor 2,000 h are

sufficient in order to forecast the degradation of a SOEC and much longer operating times are needed [13,20]. However, in order to be able to investigate the general consequence of a higher operating pressure on the long-term stability, an increased number of experiments have to be conducted in order to reproduce the results shown in this study and in order to increase the statistical significance.

List of Abbreviations and Symbols

ASR _{pol}	Area specific polarization resistance / $\Omega \text{ cm}^2$
ASR _{total}	Total area specific resistance / $\Omega \text{ cm}^2$
ASR _{Ω}	Area specific ohmic resistance / $\Omega \text{ cm}^2$
EDX	Energy-dispersive X-ray spectroscopy
EIS	Electrochemical impedance spectroscopy
ESC	Electrolyte supported cell
f	Frequency / Hz
i	Current density / A cm^{-2}
GDC	Gadolinium-doped ceria
LSCF	Lanthanum strontium cobalt ferrite
Ni	Nickel
OCV	Open circuit voltage
p	Pressure / bar
PTA	Post-test analysis
RC	Reactant conversion / %
SEM	Scanning electron microscopy
slpm	Standard liters per minute / L min^{-1}
SOC	Solid oxide cell
SOEC	Solid oxide electrolysis cell
U	Voltage / V
YSZ	Yttria-stabilized zirconia

References

- [1] S. H. Jensen, C. Graves, M. Chen, J. B. Hansen, X. Sun, *J. Electrochem. Soc.* **2016**, *163*, F1596.
- [2] M. Henke, C. Willich, J. Kallo, K. A. Friedrich, *Int. J. Hydrogen Energy* **2014**, *39*, 12434.
- [3] X. Sun, A. D. Bonaccorso, C. Graves, S. D. Ebbesen, S. H. Jensen, A. Hagen, P. Holtappels, P. V. Hendriksen, M. B. Mogensen, *Fuel Cells* **2015**, *15*, 697.
- [4] S. Santhanam, M. P. Heddrich, M. Riedel, K. A. Friedrich, *Energy* **2017**, *141*, 202.
- [5] M. Riedel, M. P. Heddrich, K. A. Friedrich, *Int. J. Hydrogen Energy* **2019**, *44*, 4570.
- [6] D. M. A. Dueñas, M. Riedel, M. Riegraf, R. Costa, K. A. Friedrich, *Chemie Ing. Tech.* **2020**, *92*, 45.
- [7] M. Riedel, M. P. Heddrich, K. A. Friedrich, *J. Electrochem. Soc.* **2020**, *167*, 024504.
- [8] L. Bernadet, G. Gousseau, A. Chatroux, J. Laurencin, F. Mauvy, M. Reytier, *ECS Trans.* **2015**, *68*, 3369.
- [9] S. Seidler, M. Henke, J. Kallo, W. G. Bessler, U. Maier, K. A. Friedrich, *J. Power Sources* **2011**, *196*, 7195.
- [10] M. P. Hoerlein, M. Riegraf, R. Costa, G. Schiller, K. A. Friedrich, *Electrochim. Acta* **2018**, *276*, 162.
- [11] M. B. Mogensen, A. Hauch, X. Sun, M. Chen, Y. Tao, S. D. Ebbesen, K. V. Hansen, P. V. Hendriksen, *Fuel Cells* **2017**, *17*, 434.
- [12] R. Knibbe, M. L. Traulsen, A. Hauch, S. D. Ebbesen, M. Mogensen, *J. Electrochem. Soc.* **2010**, *157*, B1209.
- [13] J. Schefold, A. Brisse, H. Poepke, *Int. J. Hydrogen Energy* **2017**, *42*, 13415.
- [14] P. Moçoteguy, A. Brisse, *Int. J. Hydrogen Energy* **2013**, *38*, 15887.
- [15] J. Schefold, A. Brisse, A. Surrey, C. Walter, *Int. J. Hydrogen Energy* **2020**, *45*, 5143.
- [16] C. E. Frey, Q. Fang, D. Sebold, L. Blum, N. H. Menzler, *J. Electrochem. Soc.* **2018**, *165*, F357.
- [17] D. Schäfer, Q. Fang, L. Blum, D. Stolten, *J. Power Sources* **2019**, *433*, 126666.
- [18] Q. Fang, L. Blum, N. H. Menzler, *J. Electrochem. Soc.* **2015**, *162*, F907.
- [19] V. N. Nguyen, Q. Fang, U. Packbier, L. Blum, *Int. J. Hydrogen Energy* **2013**, *38*, 4281.
- [20] Q. Fang, C. E. Frey, N. H. Menzler, L. Blum, *J. Electrochem. Soc.* **2018**, *165*, F38.
- [21] M. Lang, S. Raab, M. S. Lemcke, C. Bohn, M. Physik, *ECS Trans.* **2019**, *91*, 2713.
- [22] S. H. Jensen, X. Sun, S. D. Ebbesen, M. Chen, *Fuel Cells* **2016**, *16*, 205.
- [23] J. Brabandt, O. Posdziech, *ECS Trans.* **2017**, *78*, 2987.
- [24] M. Preininger, B. Stoeckl, V. Subotić, F. Mittmann, C. Hochenaue, *Appl. Energy* **2019**, *254*, 113695.
- [25] B. E. Mai, T. Heller, D. Schimanke, J. Lawrence, C. Wunderlich, *ECS Trans.* **2009**, *25*, 187.
- [26] S. Srikanth, M. P. Heddrich, S. Gupta, K. A. Friedrich, *Appl. Energy* **2018**, *232*, 473.
- [27] A. Hauch, S. D. Ebbesen, S. H. Jensen, M. Mogensen, *J. Electrochem. Soc.* **2008**, *155*, 1184.
- [28] X. Zhang, J. E. O'Brien, R. C. O'Brien, J. J. Hartvigsen, G. Tao, G. K. Housley, *Int. J. Hydrogen Energy* **2013**, *38*, 20.
- [29] M. Riedel, M. P. Heddrich, K. A. Friedrich, *Proc. 13th Eur. SOFC SOE Forum*, Lucerne, Switzerland, **2018**, B1504.
- [30] M. B. Mogensen, *Curr. Opin. Electrochem.* **2020**, *21*, 265.
- [31] J. Schefold, A. Brisse, F. Tietz, *J. Electrochem. Soc.* **2011**, *159*, A137.
- [32] M. Henke, C. Willich, J. Kallo, K. A. Friedrich, *Int. J. Hydrogen Energy* **2014**, *39*, 12434.
- [33] L. Bernadet, G. Gousseau, A. Chatroux, J. Laurencin, F. Mauvy, M. Reytier, *Int. J. Hydrogen Energy* **2015**, *40*, 12918.
- [34] C. Graves, S. D. Ebbesen, S. H. Jensen, S. B. Simonsen, M. B. Mogensen, *Nat. Mater.* **2015**, *14*, 239.
- [35] M. Mori, T. Yamamoto, H. Itoh, H. Inaba, H. Tagawa, *J. Electrochem. Soc.* **1998**, *145*, 1374.
- [36] J. Malzbender, W. Fischer, R. W. Steinbrech, *J. Power Sources* **2008**, *182*, 594.

- [37] M. P. Hoerlein, G. Schiller, F. Tietz, K. A. Friedrich, in *Proc. 14th Int. Symp. Solid Oxide Fuel Cells*, Glasgow, Scotland, **2015**, pp. 3553.
- [38] M. P. Hoerlein, V. Yurkiv, G. Schiller, K. A. Friedrich, in *Proc. 12th Eur. SOFC SOEC Forum*, Lucerne, Switzerland, **2016**.
- [39] M. Riedel, M. P. Heddrich, K. A. Friedrich, in *Proc. 1st Int. Conf. Electrolysis*, Copenhagen, Denmark, **2017**, pp. 71.
- [40] B. J. McBride, M. J. Zehe, S. Gordon, *NASA Glenn Coefficients for Calculating Thermodynamic Properties of Individual Species*, **2002**.
- [41] J. Schefold, A. Brisse, H. Poepke, *Electrochim. Acta* **2015**, 179, 161.
- [42] H. Nabilek, L. Blum, H. P. Buchkremer, V. Haanappel, L. G. J. B. de Haart, W. J. Quadackers, R. Steinberger-Wilckens, R. W. Steinbrech, U. Reisingen, F. Tietz, *Adv. in Solid Oxide Fuel Cells III: Ceramic and Engineering Science Proceedings*, **2009**, 28, 65.
- [43] J. E. O'Brien, C. M. Stoots, J. S. Herring, M. G. McKellar, E. A. Harvego, M. S. Sohal, K. G. Condie, *High Temperature Electrolysis for Hydrogen Production from Nuclear Energy Technology Summary*, Idaho National Laboratory, February 2010.
- [44] S. Diethelm, J. Van herle, D. Montinaro, O. Bucheli, *Fuel Cells* **2013**, 13, 631.
- [45] C. Geipel, K. Hauptmeier, K. Herbrig, F. Mittmann, M. Münch, M. Pötschke, L. Reichel, T. Strohbach, T. Seidel, A. Surrey, C. Walter, *ECS Trans.* **2019**, 91, 123.
- [46] S. D. Ebbesen, J. Høgh, K. A. Nielsen, J. U. Nielsen, M. Mogensen, *Int. J. Hydrogen Energy* **2011**, 36, 7363.
- [47] T. L. Skafte, P. Blennow, J. Hjelm, C. Graves, *J. Power Sources* **2018**, 373, 54.
- [48] G. Jeanmonod, S. Diethelm, J. Van Herle, *J. Phys. Energy* **2020**, 2, 034002.
- [49] T. Brylewski, T. Maruyama, M. Nanko, K. Przybylski, *J. Therm. Anal. Calorim.* **1999**, 55, 681.
- [50] Y. Tao, S. D. Ebbesen, M. B. Mogensen, *J. Power Sources* **2016**, 328, 452.
- [51] F. Tietz, D. Sebold, A. Brisse, J. Schefold, *J. Power Sources* **2013**, 223, 129.
- [52] M. Hubert, J. Laurencin, P. Cloetens, B. Morel, D. Montinaro, F. Lefebvre-Joud, *J. Power Sources* **2018**, 397, 240.
- [53] A. Zekri, M. Knipper, J. Parisi, T. Plaggenborg, *Phys. Chem. Chem. Phys.* **2017**, 19, 13767.
- [54] J. Mason, I. Celik, S. Lee, H. Abernathy, G. Hackett, *J. Electrochem. Soc.* **2018**, 165, F64.
- [55] L. Kröll, L. G. J. De Haart, I. Vinke, R. A. Eichel, *Phys. Rev. Appl.* **2017**, 7, 044007.
- [56] M. B. Mogensen, M. Chen, H. L. Frandsen, C. Graves, A. Hauch, T. Jacobsen, S. H. Jensen, T. L. Skafte, X. Sun, *ECS Trans.* **2019**, 91, 613.
- [57] A. Gubner, H. Landes, J. Metzger, H. Seeg, R. Stübner, *ECS Proc. Vol.* **1997**, 1997–40, 844.
- [58] C. W. Bale, E. Bélisle, P. Chartrand, S. A. Decterov, G. Eriksson, A. E. Gheribi, K. Hack, I. H. Jung, Y. B. Kang, J. Melançon, A. D. Pelton, S. Petersen, C. J. Sangster, P. Spencer, M. A. Van Ende, *Calphad Comput. Coupling Phase Diagrams Thermochem.* **2016**, 54, 35.
- [59] A. Hauch, K. Brodersen, M. Chen, M. B. Mogensen, *Solid State Ionics* **2016**, 293, 27.
- [60] M. B. Mogensen, A. Hauch, X. Sun, M. Chen, Y. Tao, S. D. Ebbesen, P. V. Hendriksen, *Proc. 12th Eur. Sofc Soe Forum* **2016**, A0902
- [61] A. Hauch, M. Mogensen, A. Hagen, *Solid State Ionics* **2011**, 192, 547.
- [62] L. Abadlia, F. Gasser, K. Khalouk, M. Mayoufi, J. G. Gasser, *Rev. Sci. Instrum.* **2014**, 85, 951211.
- [63] M. Riegraf, A. Zekri, M. Knipper, R. Costa, G. Schiller, K. A. Friedrich, *J. Power Sources* **2018**, 380, 26.
- [64] T. Jacobsen, M. Mogensen, *ECS Trans.* **2008**, 13, 259.
- [65] S. N. Rashkeev, M. V. Glazoff, *Int. J. Hydrogen Energy* **2012**, 37, 1280.
- [66] J. R. Mawdsley, J. David Carter, A. Jeremy Kropf, B. Yildiz, V. A. Maroni, *Int. J. Hydrogen Energy* **2009**, 34, 4198.
- [67] S. J. Kim, G. M. Choi, *Solid State Ionics* **2014**, 262, 303.
- [68] M. A. Laguna-Bercero, R. Campana, A. Larrea, J. A. Kilner, V. M. Orera, *J. Power Sources* **2011**, 196, 8942.
- [69] C. Graves, S. D. Ebbesen, M. Mogensen, *Solid State Ionics* **2011**, 192, 398.
- [70] M. Chen, J. V. T. Høgh, J. U. Nielsen, J. J. Bentzen, S. D. Ebbesen, P. V. Hendriksen, *Fuel Cells* **2013**, 13, 638.
- [71] S. D. Ebbesen, R. Knibbe, M. Mogensen, *J. Electrochem. Soc.* **2012**, 159, F482.